Electronic Supplementary Material (ESI) for Materials Horizons.

Supplementary Information

Lower Limits for Non-Radiative Recombination Loss in Organic Donor/Acceptor Complexes

Yun Liu[1], Zilong Zheng[2,3], Veaceslav Coropceanu[2,4], Jean-Luc Brédas[2,4], David S. Ginger[1]*

[1]Department of Chemistry, University of Washington, Seattle, WA 98195-2120, USA

[2]School of Chemistry and Biochemistry, Georgia Institute of Technology, Atlanta, Georgia 30332-0400, USA

[3]College of Materials Science and Engineering, Beijing University of Technology, Beijing 100124, China

[4]Department of Chemistry and Biochemistry, The University of Arizona, Tucson, Arizona 85721-0088, USA

Correspondence to: *David S. Ginger: dginger@uw.edu

Experimental Method

Device fabrication and characterization The device structure of optimized m-MTDATA:3TPYMB solar cells is: ITO/PEDOT:PSS (50nm)/Meo-TPD (12nm)/m-MTDATA (10nm)/m-MTDATA:3TPYMB (1:1 by mass)/3TPYMB (10nm)/Bphen (10nm)/LiF (1nm)/Al (100nm). ITO substrates were pre-etched, cleaned via sonication in micro-90 detergent, deionized water, acetone, and isopropanol solution, and plasma cleaned with O_2 for 10 min prior to spin-coating. PEDOT:PSS was spin-coated at 4000 rpm for 40 s, followed by annealing at 150°C for 15 min. All following layers were deposited via thermal evaporation. For codeposition of m-MTDATA and 3TPYMB, the 1:1 mass ratio was achieved via controlling deposition rate.

For external quantum efficiency measurement, excitation light was produced by a monochromated Tungsten-Halogen lamp and was modulated at 220 Hz using a Stanford Research Systems SR450 Chopper Controller. Photocurrent was detected by a Stanford Research Systems SR830 Lock-in Amplifier referenced to the chopper controller. External quantum efficiency was calculated using a calibrated photodiode. Pixel mask was used to minimize edge effect, and the irradiation area on the pixel was ~0.06cm^2.

We performed variable angle spectroscopic ellipsometry (VASE) measurement to calculate the fraction of light absorbed by the m-MTDATA:3TPYMB layer in the device. VASE measures the change in polarization, both the amplitude ratio Ψ and the phase difference Δ, as light from various incidence angles reflects or transmits from the material. Spectra of Ψ and Δ were measured on m-MTDATA:3TPYMB blend co-deposited onto silicon substrates with 300 nm thermally grown SiO_2, at 3 different incidence angles (55°, 65° and 75°). The complex refractive indices n and k were modeled using a B-Spline model via the CompleteEASE software from J.A. Woollam Co. A transfer-matrix algorithm was used to calculate the fraction of light absorbed in each layer of the solar cell device.[1] To calculate IQE_{PV}, the EQE_{PV} spectrum was divided by the fraction of absorbed light in the m-MTDATA:3TPYMB layer.

The current density-voltage curve was measured with a Keithley 2400 source meter upon illumination of a 385nm LED on the same irradiation area as EQE measurement. The intensity of the LED illumination was corrected to AM1.5G 1-Sun intensity by spectrally matching to the solar spectrum.

EL spectrum was measured on the same m-MTDATA:3TPYMB device used for EQE and J-V measurement. The device was mounted inside a chamber under dynamic vacuum and was held at a constant bias (Keithley 2400) that corresponded to the short-circuit charge density at AM1.5G illumination. The electroluminescence was collected and focused into a spectrograph (MS-2300i, Princeton Instruments) using F/# matched optics and the spectra were measured using a LN2-cooled Si array CCD detector (Spec-10, Princeton Instruments). The spectra were corrected for the instrument response using a calibrated white light source (HL-P-CAL-EXT, Ocean Optics).

EL quantum yield was measured on a home-built set-up inside a N_2 glovebox. The device was mounted onto a holder inside a light-tight enclosure, with glass side facing a large area Si photodiode (Hamamatsu S3204-08). The holder was designed such that waveguided emission was blocked from the detector.

Photoluminescence characterization

PL decay kinetics of the blend film were measured using a Hamamatsu streak camera with a slow-scan unit. Samples used in trPL experiments were prepared on glass substrates using the protocol described above and were kept under dynamic vacuum during measurement. Film samples were irradiated with 365 nm pulse pumped at 1 kHz from a Coherent Inc./Light Source OPerA optical parametric amplifier. PL decay of the m-MTDATA and 3TPYMB solution (0.016M) was measured using a time-correlated single photon counting system (Picoharp 300) using a 375nm pulsed laser (PDL-800) as excitation source.

Steady-state PL measurement was performed on m-MTDATA:3TPYMB device on a home-built set-up. A 374 nm solid-state laser was used for excitation. The sample was mounted in a chamber and placed at a 45-degree angle from the laser beam path. The photoexcitation was focused onto one specific pixel from the glass side. PL emission was focused onto a fiber-coupled OceanOptics USB2000+ CCD spectrometer. A 500 nm (cut-on) filter was used in front of the detector to block the scattered laser excitation. The spectral response of the detector was corrected with the spectrum of a calibrated white-light source taken in the same optical geometry as PL measurements of the sample. Low-temperature PL spectrum was measured by mounting samples in a cryostat (Janis Research Co., STVP-100) with a temperature controller (Lakeshore 332).

PL quantum efficiency of m-MTDATA:3TPYMB thin film was measured with a Hamamatsu C9920-2 integrating sphere system. The film was photoexcited with 365nm beam generated from monochromated lamp. The excitation intensity and sample photoluminescence were simultaneously measured using a CCD spectrometer (Hamamatsu C10027). Three measurements were made (sample in the light path, sample out of the light path, and sample removed) and PLQY was calculated using the method of de Mello *et al*.[2] PL quantum efficiency of m-MTDATA and 3-TPYMB solution (0.016M) was measured in the same set-up.

Section S1 PL kinetics of m-MTDATA:3TPYMB

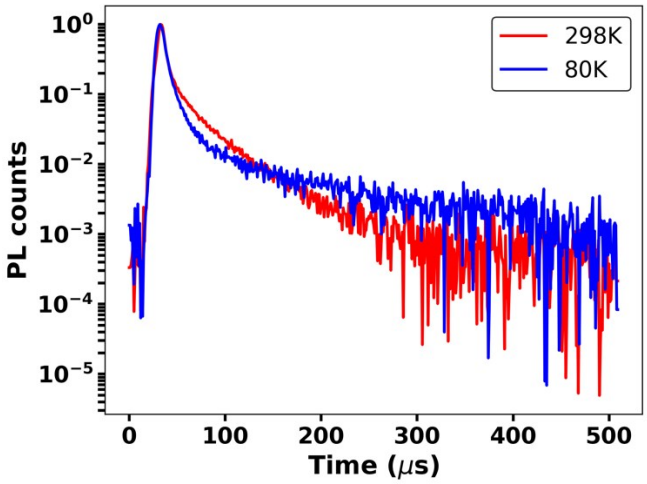

Figure S1. PL decay of m-MTDATA:3TPYMB at 80K and 298K.

The temperature-dependent PL kinetics are influenced by the rates for intersystem crossing, reverse intersystem crossing, and non-radiative recombination of the singlet and triplet states.[3] **Figure S1** shows that the prompt and delayed components both vary with temperature. Compared to room temperature kinetics, the delayed component slows down significantly at lower temperature as reverse ISC, the rate-limiting step,[3] slows down. The PL kinetics contain a delayed component even at 80 K, which is expected given the small ΔE between singlet CT and triplet LE based on our theoretical calculations (Figure 5b) and previous reports.[3,4]

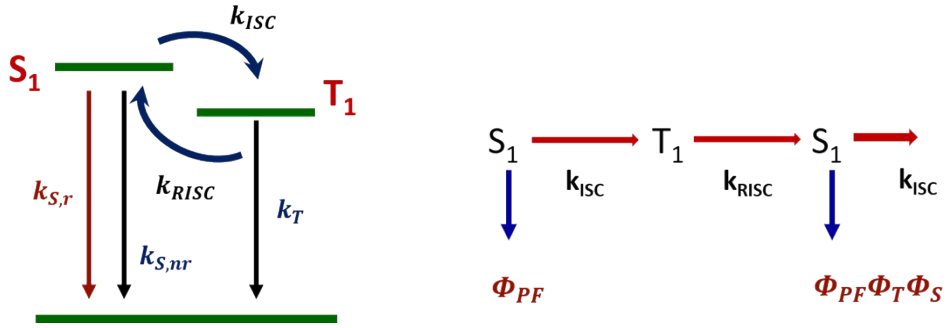

The kinetics of TADF-emissive states can be described via the scheme above.[3] To calculate the parameters of interest ($k_{s,r}$, $k_{s,nr}$, k_{ISC}), we first write the prompt PL yield (Φ_{PF}), the triplet and singlet yields (Φ_T and Φ_S), and total PL yield (Φ_F) as:

$$\Phi_{PF} = \frac{k_{s,r}}{k_{s,r} + k_{s,nr} + k_{ISC}} = k_{s,r}\tau_{PF} \quad (1)$$

$$\Phi_T = \frac{k_{ISC}}{k_{s,r} + k_{s,nr} + k_{ISC}} = k_{ISC}\tau_{PF} \quad (2)$$

$$\Phi_S = \frac{k_{RISC}}{k_{s,r} + k_{RISC}} \sim 1 \; assuming \; k_T \ll k_{RISC} \quad (3)$$

$$\Phi_F = \Phi_{PF} + \Phi_{DF} = \Phi_{PF} + \Phi_{PF}\Phi_T\Phi_S + \Phi_{PF}\Phi_S^2\Phi_T^2 + \Phi_{PF}\Phi_S^3\Phi_T^3 + \cdots \quad (4)$$

From (4), we obtain:

$$\Phi_F = \frac{\Phi_{PF}}{1 - \Phi_S\Phi_T} \quad (5)$$

$$\Phi_{DF} = \frac{\Phi_{PF}\Phi_S\Phi_T}{1 - \Phi_S\Phi_T} \quad (6)$$

$$\frac{\Phi_{DF}}{\Phi_{PF}} = \frac{\Phi_S\Phi_T}{1 - \Phi_S\Phi_T} \quad (7)$$

Substitution of (3) and (2) into (7), we get:

$$\frac{\Phi_{DF}}{\Phi_{PF}} = \frac{k_{ISC}\tau_{PF}}{1 - k_{ISC}\tau_{PF}} \quad (8)$$

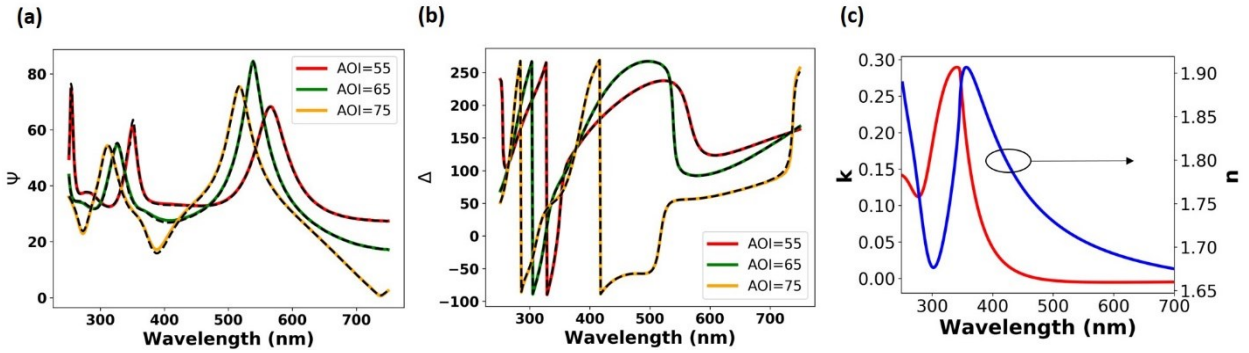

Figure S2. Fitting of the ellipsometry data of the m-MTDATA:3-TPYMB blend: (a) Ψ and (b) Δ at three angles of incidence (AOI). Refractive indices n and k are shown in (c).

Section S2 Voltage loss analysis

The open-circuit voltage loss can be separated into the following terms[5], based on the deviation of the actual short-circuit current J_{SC} and dark saturation current J_0 from their ideal values ($J_{SC}^{SQ}$and J_0^{SQ}) at the Shockley-Queisser limit[6] (Eqn. S1-3). V_{OC}^{SQ} is the ideal open-circuit voltage in the Shockley-Queisser limit, which assumes EQE_{PV} to be a step-function that equals unity above bandgap and zero below bandgap.[6] ΔV_{OC}^{SC} is the voltage loss due to a non-ideal charge generation.[7,8] At low photon energies, the blackbody radiation spectrum increases in intensity, resulting in excess absorption by the solar cell and thus, based on Kirchhoff's radiation theorem, equivalent emission from the solar cell to the ambient. This absorption edge broadening results in additional radiative recombination and thus voltage loss, namely the radiative recombination voltage loss (ΔV_{OC}^{r}).[7,8] The last loss term $\Delta V_{OC}^{nr}$is due to non-radiative recombination of photogenerated charges, and is thus determined by the electroluminescence efficiency (EQE_{EL}):

$$V_{OC} = \frac{kT}{q}\ln\left(\frac{J_{sc}}{J_0}\right) \quad \text{Eqn. S1}$$

$$V_{OC} = \frac{kT}{q}\ln\left(\frac{J_{SC}^{SQ}}{J_0^{SQ}} * \frac{J_{SC}}{J_{SC}^{SQ}} * \frac{J_0^{SQ}}{J_0^{rad}} * \frac{J_0^{rad}}{J_0}\right) \quad \text{Eqn. S2}$$

$$V_{OC} = V_{OC}^{SQ} + \Delta V_{OC}^{SC} + \Delta V_{OC}^{r} + \Delta V_{OC}^{nr} \quad \text{Eqn. S3}$$

We now briefly describe the procedure for calculating each voltage term, which has been detailed in previous work.[5,8]

1. V_{OC}^{SQ}: We first evaluate the bandgap (E_g) as the average of the probability distribution of E_g calculated from the first derivative of the EQE_{PV} onset (Eqn. S4). We determine this value to be 3.239eV,[9] which corresponds to an ideal V_{OC} of 2.85V in the Shockley-Queisser limits at 295K.[6]

$$E_g = \int_a^b E_g P(E_g) dE_g \Big/ \int_a^b P(E_g) dE_g \quad \text{Eqn. S4}$$

where a and b are the FWHM limits of $P(E_g)$

2. ΔV_{OC}^{SC}: We evaluate the actual short-circuit current (J_{SC}) and the Shockley-Queisser J_{SC}^{SQ} via Eqn S5. For J_{SC}^{SQ}, EQE_{PV} is represented by a Heaviside function with onset at E_g. For J_{SC} the experimental EQE_{PV} is used.

$$J_{SC} = q\int_{E_g}^{\infty} EQE_{PV}(E)\phi_{AM1.5}(E)dE \qquad \text{Eqn. S5}$$

3. ΔV_{OC}^{r}: We evaluate J_0^{SQ} and J_0^{rad} based on Eqn. S6. To calculate J_0^{SQ}, EQE_{PV} is represented by a Heaviside function with onset at E_g. For J_0^{rad}, the experimental EQE_{PV} spectrum was extended to the lower-energy region based on Rau's reciprocity theorem.[8,10] Within the framework of Rau's reciprocity theorem, EQE_{PV} and EL spectra are related via the blackbody radiation spectrum (Eqn. S7), because photogenerated free charges must radiatively recombine. First, we test the reciprocity theorem by recreating the sub-gap tail of the EQE_{PV} spectrum with the blackbody radiation spectrum at 295 K and the EL spectrum measured at 1 Sun equivalent injection current condition. Figure 3c in the main text shows that although the large shift of the EL spectrum from absorption limits the overlapping wavelength range between EL onset and EQE_{PV} tail, the recreated sub-gap EQE_{PV} tail follows the overall trend of the experimental EQE_{PV} spectrum and overlays very well over the measured EQE_{PV} tail. Using the recreated EQE_{PV} spectrum, we then estimated the radiative saturation current, and the radiative recombination loss given a non-step function absorption edge and obtain $\Delta V_{OC}^{r} = 0.600\ V$.

$$J_0 = q\int_{0}^{\infty} EQE_{PV}(E)\phi_{BB}(E)dE \qquad \text{Eqn. S6}$$

$$\phi_{EL}(E) = EQE_{PV}(E)\phi_{BB}(E)\left(\exp\left(\frac{qV}{kT}\right) - 1\right) \qquad \text{Eqn. S7}$$

4. ΔV_{OC}^{nr}: We determined EQE_{EL} of the solar cell device to be 1.67% at injection current equivalent to J_{SC} at AM1.5G illumination intensity. Based on Eqn. 2 in the main text, ΔV_{OC}^{nr} is thus 0.104 V. Taken together, our voltage loss analysis leads to an estimated V_{OC} of 2.10 V, which agrees quantitatively with our measured value of 2.11 V (Table 1 in main text).

Section S3. PL spectra of m-MTDATA, 3TPYMB and m-MTDATA: 3TPYMB

The transition dipole moments are calculated using the equation below.[11] Parameters are obtained from PLQY, steady-state PL spectroscopy and PL lifetime measurements on the m-MTDATA:3TPYMB blend film and dilute m-MTDATA and 3TPYMB solutions. To determine the LE adiabatic energies of the single components, we took the intersection of the normalized PL and absorption spectra (Figure S5).[12]

$$k_r = \frac{64\pi^4 E_{em}^3 d_{LE}^2}{3h^4 c^3} \qquad \text{Eqn. S8}$$

d_{LE}: transition dipole moment from LE state to the ground state

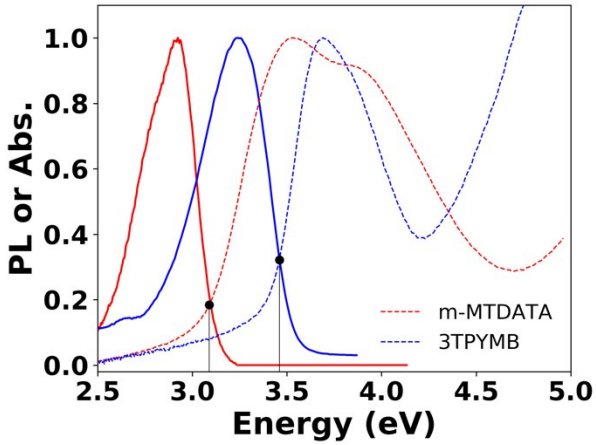

Figure S3. Normalized absorption and PL spectra of m-MTDATA and 3TPYMB.

Table S1. Summary of molecular and photoluminescence parameters.

	m-MTDATA	3TPYMB	m-MTDATA:3TPYMB blend
E_{em} (eV)	2.9	3.2	2.18
PLQY	0.109	0.067	0.128
τ_{mono} (s)	2.12×10^{-9}	1.04×10^{-9}	4.7×10^{-6} (prompt)
k_r (s-1)	5.14×10^{7}	6.44×10^{7}	2.72×10^{4}
k_{nr} (s-1)	4.2×10^{8}	8.97×10^{8}	1.86×10^{5}
$d_{LE\ or\ CT}$ (D)	3.58	3.46	0.049

Section S4. Marcus-Levich-Jortner framework (a two-state model)

1. Theory background and derivation

In the Marcus-Levich-Jortner (MLJ) framework, the radiative and non-radiative recombinations of the CT states are described as an electron-transfer event between the CT and ground states (Figure S2); the portion of the reorganization energy due to high-energy vibrational modes (λ_{qm}) and the contribution to the reorganization energy (λ_c) related to low-frequency vibrations are treated quantum-mechanically and classically, respectively.

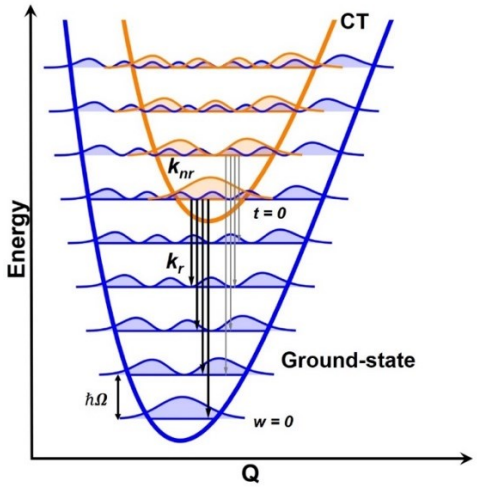

Figure S4. Potential energy surfaces of the CT state (orange) and the ground state (blue); the harmonic oscillator vibrational levels are given with quantum numbers *t* and *w*, respectively. The vibronic wavefunctions are illustrated by the color-shaded curves. The radiative transitions are indicated by arrows and the non-radiative transitions are shown as vibrational wavefunction overlap. The vibrational spacing is denoted as $\hbar\Omega$.

In the MLJ framework, the non-radiative transition rate can be written as:

$$k_{nr} = \frac{2\pi}{\hbar} V_{CT-G}^{2} FCWD(0) \qquad \text{Eqn. S9}$$

where $V_{CT\text{-}G}$ is the electronic coupling between the CT state and ground state; the Franck-Condon weighted density of states (FCWD) factor is given by:

$$FCWD(\hbar\omega) = \frac{1}{\sqrt{4\pi\lambda_c k_B T}} \sum_{w=0}^{\infty} \frac{e^{-S_{qm}} S_{qm}^{w}}{w!} e^{\frac{-\left(E_{CT}-\lambda_c - w\hbar\omega_{qm} - \hbar\omega\right)^2}{4\lambda_c k_B T}} \qquad \text{Eqn. S10}$$

where E_{CT} is the adiabatic energy of the CT state; S_{qm} and ω_{qm} ($\lambda_{qm} = S_{qm}\omega_{qm}$) denote the Huang-Rhys factor and the energy of the effective quantum vibrational mode.

Within the MLJ framework, the intensity and shape of the CT emission band are given by: [7]

$$I_r(\hbar\omega) = \frac{64\pi^4 \hbar\omega^3 d_{CT-G}^{2}}{3h^4 c^3} FCWD(\hbar\omega) \qquad \text{Eqn. S11}$$

We note that it is common to express in Eqn. S11 the transition dipole moment, d_{CT-G}, via $V_{CT\text{-}G}$ and the difference between the CT and G state dipole moments Δd_{CT-G} by using the Mulliken-Hush expression (Eqn. 3). The radiative rate constant of the CT band can then be obtained by integration of Eqn. S12:

$$k_r = \int I_r(\hbar\omega) d\hbar\omega \qquad \text{Eqn. S12}$$

Finally, the PLQY is calculated as:

$$PLQY = \frac{k_r}{k_r + k_{nr}} \qquad \text{Eqn. S13}$$

In Eqn. S13, k_{nr} accounts for all non-radiative pathways.

2. Range of parameters in energy gap law calculation

Based on previously reported parameter ranges,[13] we varied λ_c, λ_{qm}, Δd_{CT-G}, V_{CT-G}^2 and ω_{qm} individually when calculating the transition rates as a function of E_{CT}. The default value and range of variation of each parameter are shown in the table below.

	Default value	Range
E_{CT} (eV)	-	0.6-2.7
λ_c (eV)	0.15	0.1-0.4
λ_{qm} (eV)	0.15	0.05-0.4
ω_{qm} (eV)	0.15	
Δd_{CT-G} (D)	6	4-20
V_{CT-G}(eV)	0.01	1e-3–1e-1

3. Discussion

As shown in Figure S4, the experimentally determined non-radiative voltage loss of polymer/non-fullerene acceptor,[5,14–20] polymer/fullerene,[18,20–24] and OLED-based OPVs[24] lie within the calculation range (Table S2). Importantly, for high-energy CT systems such as the TADF-based system in this study and for OLED-material-based systems, the non-radiative transition rates can vary by many orders of magnitude. The radiative transition rates demonstrate a less dramatic response (Figure S3) and vary by some 2-3 orders of magnitude as a function of reasonable modulations of the reorganization energies and changes in dipole moments throughout the range of E_{CT} we explored (0.6-2.7 eV). In contrast, for systems with low-energy CT states (0.5-1.0 eV), the non-radiative rates vary considerably more. We note that the charge-transfer states in most polymer/NFA blends are around 1.0-1.5 eV.[5,14–24] In this energy range, the non-radiative rates can vary by factors up to 10^4-10^8 for reasonable values of the reorganization energy and other parameters. For higher E_{CT} systems, such as the TADF-emissive blend herein, the non-radiative

rate is extremely sensitive to changes in the reorganization energy. These observations confirm that it is crucial (1) to control the reorganization energy in CT systems in order to reduce the non-radiative voltage loss and (2) to use appropriate microscopic parameters when discussing experimental rates and voltage losses in the framework of the two-state MLJ model.

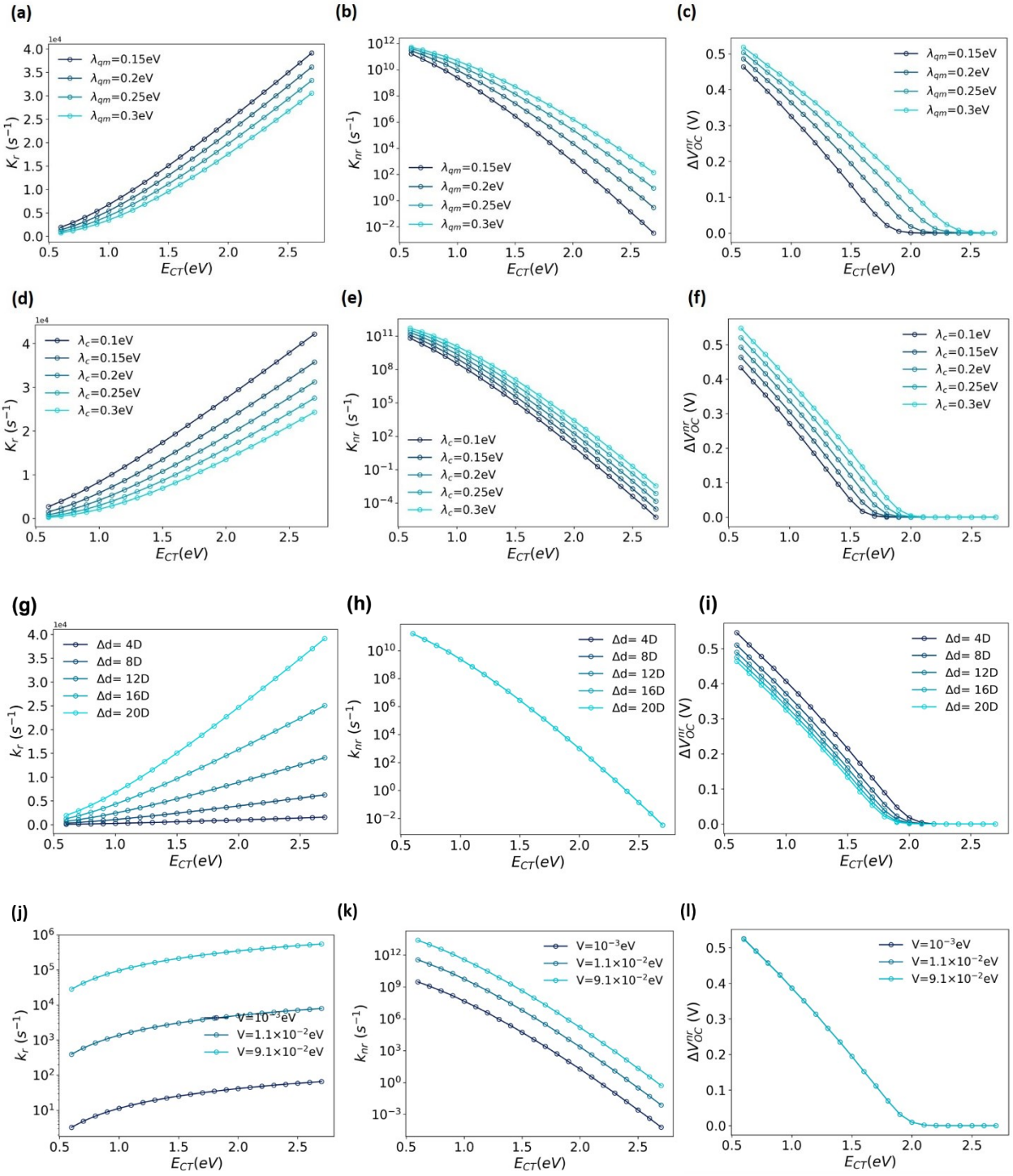

Figure S5. Effect on k_r, k_{nr} and ΔV_{OC}^{nr} as a function of E_{CT} upon varying (a)-(c) λ_{qm}, (d)-(f) λ_c, (g)-(i) the change in dipole moment Δd_{CT-G} and (j)-(l) the electronic coupling V_{CT-G}.

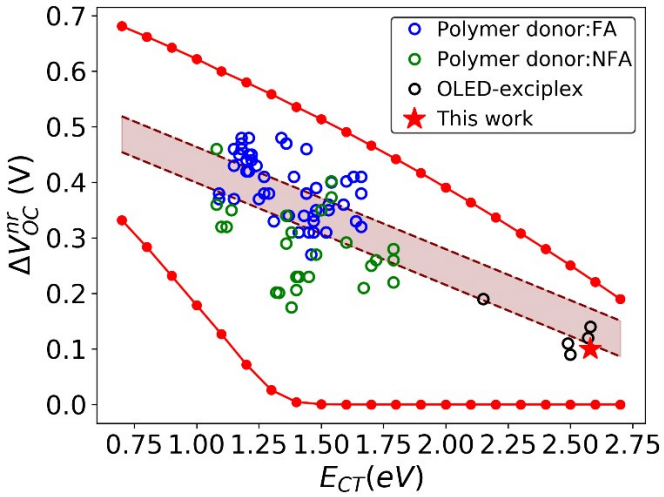

Figure S6. Expanded "energy gap law" (with the upper and lower limit for ΔV_{OC}^{nr} at a certain E_{CT} shown in red) for ΔV_{OC}^{nr} as a function of E_{CT}. Parameters used to compute the lower curve are: λ_{qm}= 0.05 eV, λ_c=0.1 eV, Δd_{CT-G}=20 D, V_{CT-G}=0.001 eV, ω_{qm}=0.15 eV, and parameters for the upper curve are: λ_{qm}= 0.4 eV, λ_c=0.4 eV, Δd_{CT-G}=4 D, V_{CT-G}=0.1 eV, ω_{qm}=0.15 eV. The shaded area represents the range calculated for ΔV_{OC}^{nr} based on a linear relation between ΔV_{OC}^{nr} and $E_{CT} - \lambda_c$.[23]

Section S5. Molecular-dynamics simulations and electronic-structure calculations

The morphology of the m-MTDATA/3TPYMB blend was derived by means of molecular dynamics (MD) simulations based on the all-atom optimized potentials for liquid simulations (OPLS-AA) force field.[25] The point charges for the carbon, oxygen, sulfur, nitrogen, and hydrogen atoms of the donor/acceptor molecules were obtained via DFT calculations and employed for the MD simulations. These parameters were shown to provide adequate packing density when compared to experimental values.[26] The methodology consists of randomly placing 250 molecules each of donor and acceptor in a simulation box at a very low density of less than 0.1 g/cm^3. An NVT simulation was carried out at 1000 K for at least 1 ns followed by at least 5-ns isobaric-isothermal ensemble simulations at 1 bar and 300 K. A time step of 1 fs was used to integrate Newton's equations of motion.

Excited-state calculations were performed by means of time-dependent DFT (TDDFT) based on the Tamm-Dancoff approximation (TDA). We used the tuned range-separated SRSH-ωPBE-D3 functional and the 6-31G(d) basis set. Geometry optimizations of the donor and acceptor molecules were carried out at the same SRSH-ωPBE-D3/6-31G(d) level. Tuning of the range-separated parameters (ω) was conducted by minimizing the error function J(ω):[27]

$$J(\omega) = [\epsilon_{HOMO}(\omega) - IP(\omega)]^2 + [\epsilon_{LUMO}(\omega) - EA(\omega)]^2$$

Here, ϵ_{HOMO} and ϵ_{LUMO} are the energies of the highest occupied and lowest unoccupied molecular orbitals (HOMO and LUMO); IP and EA denote the vertical first ionization potential and electron affinity of the system. A value of 0.10 bohr^{-1} was derived for the optimal value of ω.

The electronic couplings between the CT states and the ground and local-exciton states were calculated by means of the fragment charge difference method.[28]

The excited-state calculations were performed with the Q-chem 4 package and the MD simulations, with the GROMACS software.[29,30] A dielectric constant of 3 was used in the electronic-structure calculations.

Section S6. PL emission spectrum simulation

We have simulated the PL emission spectrum based on the MLJ two-state model (Eqn. S11) and compared it with the experimental PL spectrum. We fixed E_{CT} at the experimental 2.58 eV value, $\hbar\Omega$ at 0.10 eV and λ_t at 0.4 eV. The Huang-Rhys factor is then varied to obtain the spectral peak position overlapping with the experimental spectrum. Static disorder (represented by σ), which leads to inhomogeneous broadening of the transition linewidth, is also considered.[31,32]

We show in Figure S5b that when λ_t is greater than 0.4 eV, the simulated PL spectrum becomes significantly broader than the experimental spectrum. Figure S5a demonstrates that (1) taking λ_{qm} as 0.39 eV leads to the correct spectral shape and (2) the consideration of static disorder σ is required to obscure the vibronic envelope. We note that, as previously shown, neglecting the static disorder term would lead to miscalculations of the reorganization energy and CT-state energy.[33] For the sake of completeness, in Figure S6a-b, we compare k_{nr} and k_r calculations with and without σ; the results show that σ has a negligible effect on the rates.

In Figure 4a, we used an E_{CT} value of 2.65 eV. To evaluate the effect of E_{CT} on the simulation, we performed the same calculation as shown in Figure S6c-d. Our findings described in the main text, *i.e.,* that the k_{nr} values obtained from the two-state calculations do not agree with the experimental data, hold true.

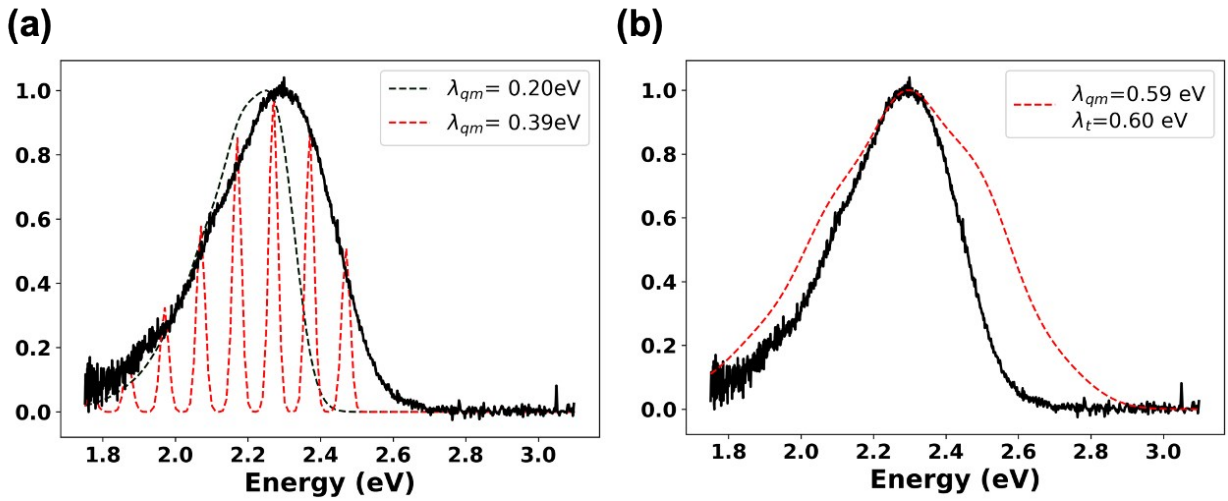

Figure S7. Simulated PL spectra obtained with the following parameters: **(a)** λ_t =0.4 eV, σ_s=0, $\omega_{qm} = 0.1\ eV$, E_{CT}=2.58 eV, λ_{qm}=0.20 eV (black) or 0.39 eV (red), and **(b)** λ_{total} =0.6 eV, σ_s=70 meV, $\omega_{qm} = 0.1\ eV$, E_{CT}=2.7 eV, λ_{qm}=0.59 eV.

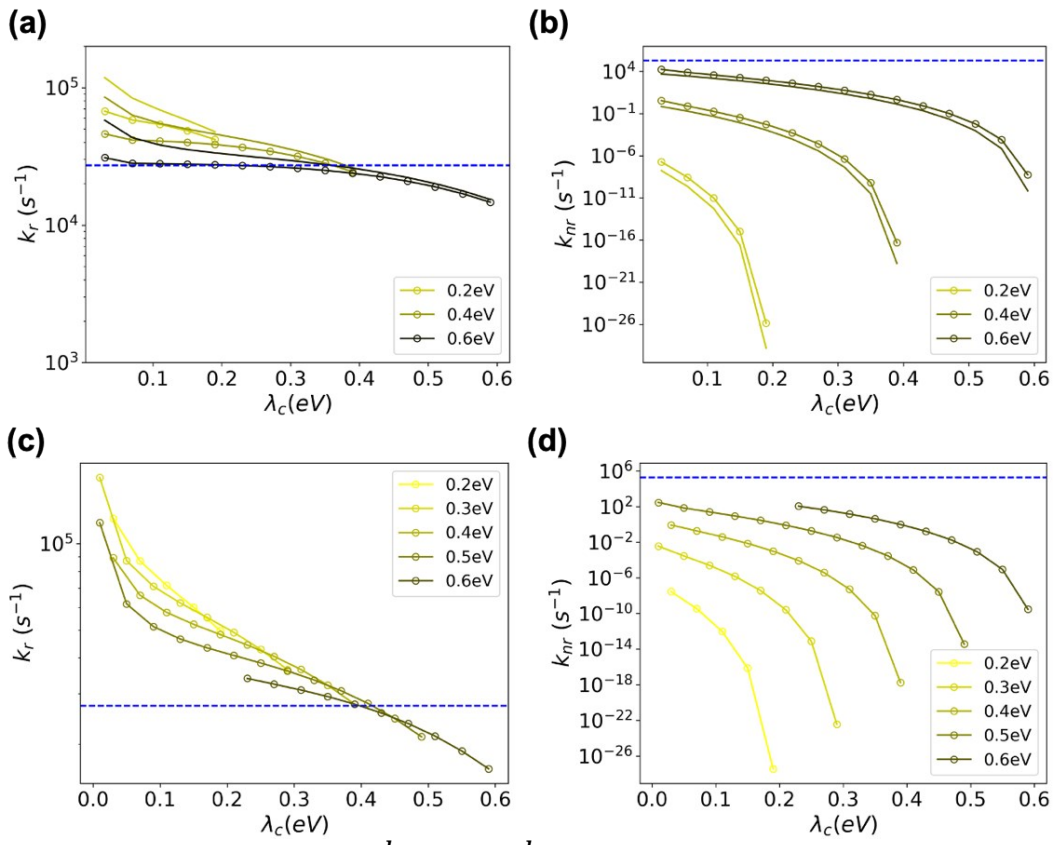

Figure S8. Comparison of **(a)** k_r and **(b)** k_{nr} using E_{CT}=2.58 eV, as a function of λ_c, with (-) and without (-o-) static disorder in Eqn. S9. We calculated k_r and k_{nr} using λ_t of 0.2 eV, 0.4 eV and 0.6 eV (shown in legend) and varied the fraction of λ_c within λ_t shown on the x-axis. The line traces are shown in Figure 4b of the main text. **(c)** k_r and **(d)** k_{nr} calculations using E_{CT}=2.65 eV while varying λ_t from 0.2 to 0.6 eV (as indicated by the legend) and varying the fraction of λ_c within λ_t shown on the x-axis.

Section S7. PL properties of the CT state in the three-state model

We have calculated k_r, k_{nr} and PLQY for a range of CT energies using the three-state model described in the main text. In the calculations shown in the main text figure, we fixed the values of all microscopic parameters, except E_{CT}. For the E_{LE} we used the adiabatic energy of m-MTDATA of 3.09 eV.

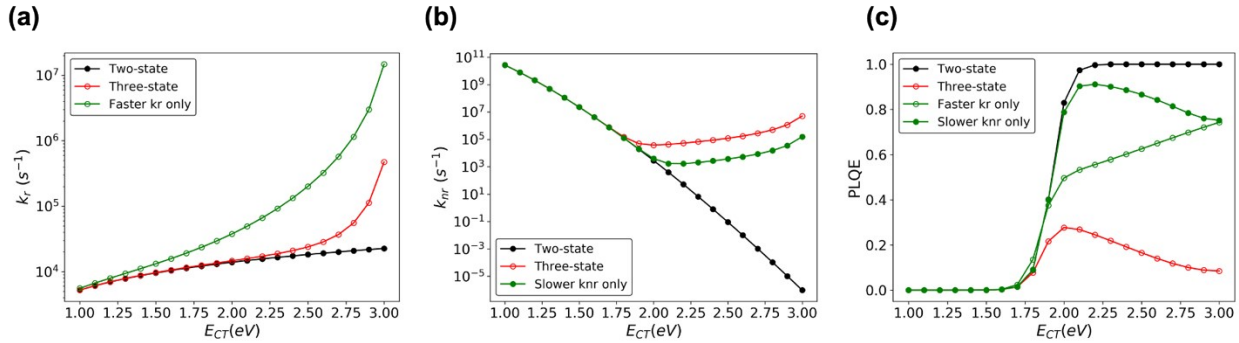

Figure S9. k_r, k_{nr} and PLQY of the CT state calculated for a range of CT energies when the PLQY of the LE state is varied. Black: Two-state calculation. Red: Three-state calculation where the PLQY of the LE state is set to10%. Green: Three-state calculation where the PLQY of the LE state is 80%. The results for the LE PLQY of 80% were achieved by starting with the parameters used in the case of LE PLQY=10% and: (1) by increasing the LE k_r or (2) by decreasing LE k_{nr} to reach LE PLQY=80%.

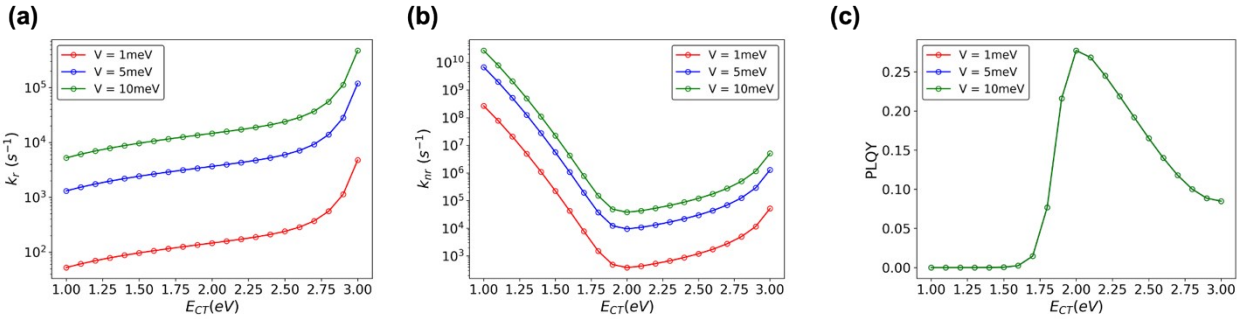

Figure S10. k_r, k_{nr} and PLQY of the CT state calculated for a range of CT energies when the CT-G and CT-LE electronic couplings vary from 1 to 5 and to 10 meV. The PLQY of the LE state is set to 10%.

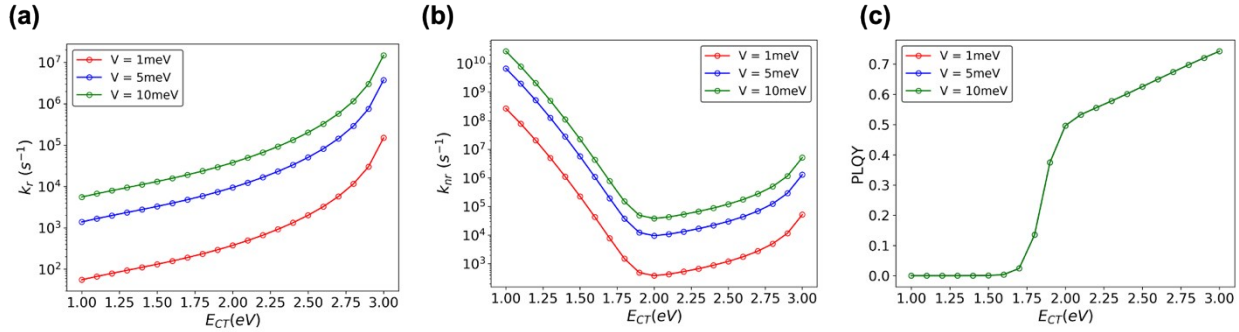

Figure S11. k_r, k_{nr} and PLQY of the CT state calculated for a range of CT energies when the CT-G and CT-LE electronic couplings vary from 1 to 5 and to 10 meV. The PLQY of the LE state is set to 80%.

Table S2. Overview of E_{CT}, PLQY, k_r and k_{nr} values reported for the CT states in donor/acceptor OPV blends. E_{CT} is determined either by fitting EQE_{PV} tail and EL spectra to a set of Gaussians (†), or by determining the intersection between the normalized absorption and PL spectra (‡). Systems in Ref. 34 are reported to show CT-LE hybridization that increases k_r. λ_{tot} obtained from EQE_{PV} and EL fitting (* indicates the numbers were tabulated from the original published figure).

	E_{CT}	λ_{tot}	PLQY	k_r (s^{-1})	k_{nr} (s^{-1})	Ref
m-MTDATA:3TPYMB	2.58†	0.41	0.128 (prompt)	2.75E+04	1.87E+05	This work
PIDSe-PhQ:PCBM	1.35†	0.19*	9.1E-05	1.08E+05	1.19E+09	[34]
PIDT-PhQ:PCBM	1.41†	0.19*	1.3E-04	9.71E+04	7.25E+08	[34]
PIDT-PhanQ:PCBM	1.43†	0.19*	1.9E-04	1.47E+05	7.81E+08	[34]
PIDSe-PhanQ:PCBM	1.42†	0.19*	2.2E-04	2.99E+05	1.39E+09	[34]
PCE10:FIDTT-2PDI	1.6†	0.15	1.4E-04	3.43E+05	2.52E+09	[5]
PNOz4T:PC71BM	1.58‡	--	8.0E-03	2.32E+07	2.88E+09	[35]
PDCBT-2F:IT-M	1.67‡	--	1.2E-02	1.58E+08	1.30E+10	[35]
PTB7-Th:IEICO	1.67‡	--	7.0E-03	9.94E+07	1.41E+10	[35]
PBQ-QF:IEICO-4F	1.36‡	--	1.0E-04	4.38E+06	4.38E+10	[35]
PvBDTTAZ:O-IDTBR	1.7‡	--	1.2E-02	1.75E+08	1.44E+10	[35]

Table S3. Overview of E_{CT} and ΔV_{nr} values reported for donor/acceptor OPV blends.

Polymer:NFA	**E_{CT}**	**ΔV_{nr}**	**Ref**
PCE10:FIDTT-2PDI	1.6	0.292	[5]
P3TEA:SF-PDI2	1.72	0.26	[36]
PBDB-T:ITIC	1.5	0.35	[14]
PDCBT-2F:IT-M	1.67	0.21	[35]
PTB7-Th:IEICO	1.45	0.23	[35]
PBQ-QF:IEICO-4F	1.36	0.29	[35]
PvBDTTAZ:O-IDTBR	1.7	0.25	[35]
BDT-ffBX-DT:SFPPDI	1.79	0.22	[19]
BDT-ffBX-DT:PDI4	1.79	0.28	[19]
BDT-ffBX-DT:PDI6	1.79	0.26	[19]
PBDB-T:NCBDT	1.54	0.373	[16]
PBDB-T:NCBDT	1.54	0.402	[16]
P6:Y11	1.38	0.175	[18]
P6:Y11	1.33	0.201	[18]
P6:Y11	1.32	0.202	[18]
PBDB-TF:BTP-4F	1.4	0.23	[37]
PBDB-TF:BTP-4Cl	1.4	0.206	[37]
D-0F:8C-ITIC	1.12	0.32	[20]
D-2F:8C-ITIC	1.38	0.31	[20]
D-4F:8C-ITIC	1.41	0.23	[20]
D-0F:ITIC	1.1	0.32	[20]
D-2F:ITIC	1.36	0.34	[20]
D-4F:ITIC	1.48	0.27	[20]
D-0F:IT-4F	1.08	0.46	[20]
D-2F:IT-4F	1.08	0.36	[20]
D-4F:IT-4F	1.14	0.35	[20]
Polymer:fullerene	**E_{CT}**	**ΔV_{nr}**	**Ref**
PIPCP:PC61BM	1.46	0.27	[23]
DCV5T-Me:C60	1.47	0.31	[24]
PM6:PCBM	1.6	0.402	[24]
APFO3:PC61BM	1.64	0.33	[23]
APFO3:PC61BM	1.66	0.38	[23]
APFO3:PC61BM	1.66	0.32	[23]
APFO3:PC71BM	1.63	0.41	[23]
APFO3:PC71BM	1.66	0.41	[23]
Dihexyl-PTV:PC61BM	1.22	0.45	[23]
High-Tg-PPV:PC61BM	1.44	0.38	[23]

LBPP5:PC71BM	1.39	0.41	[23]
MDMO-PPV:PC61BM	1.41	0.31	[23]
MDMO-PPV:PC61BM	1.47	0.34	[23]
MDMO-PPV:PC61BM	1.53	0.35	[23]
MDMO-PPV:PC61BM	1.53	0.36	[23]
MDMO-PPV:PC61BM	1.52	0.31	[23]
OC9-PEO-PPV:PC61BM	1.34	0.48	[23]
P34T:PC61BM	1.18	0.48	[23]
P34T:PC61BM	1.15	0.46	[23]
P35T:PC61BM	1.21	0.42	[23]
P35T:PC61BM	1.18	0.46	[23]
P35T:PC61BM	1.17	0.45	[23]
P35T:PC61BM	1.15	0.43	[23]
P36T:PC61BM	1.24	0.43	[23]
P36T:PC61BM	1.22	0.44	[23]
P36T:PC61BM	1.21	0.45	[23]
P36T:PC61BM	1.2	0.44	[23]
P3HT:PC61BM	1.37	0.34	[23]
P3HT:PC61BM	1.2	0.42	[23]
ReRa-P3HT:PC61BM	1.47	0.33	[23]
PBDTTPD:PC71BM	1.54	0.4	[23]
PCDTBT:PC71BM	1.48	0.39	[23]
PCPDTBT:PC71BM	1.29	0.38	[23]
PCPDTBT:PC71BM	1.25	0.37	[23]
TQm6:PC71BM	1.45	0.31	[23]
TQm8:PC71BM	1.48	0.35	[23]
TQmEH:PC71BM	1.43	0.34	[23]
TQp6:PC71BM	1.21	0.48	[23]
TQp8:PC71BM	1.27	0.41	[23]
TQp12:PC71BM	1.31	0.33	[23]
D-0F:Bis-5.1-PCBM	1.18	0.47	[20]
D-2F:Bis-5.1-PCBM	1.44	0.46	[20]
D-4F:Bis-5.1-PCBM	1.59	0.36	[20]
D-0F:PC70BM	1.15	0.37	[20]
D-2F:PC70BM	1.27	0.38	[20]
D-4F:PC70BM	1.44	0.38	[20]
D-0F:C60C70	1.09	0.38	[20]
D-2F:C60C70	1.09	0.37	[20]
D-4F:C60C70	1.36	0.47	[20]
OLED-based	**E_{CT}**	**ΔV_{nr}**	**Ref**

BF-DPB:TmPPPyTz	2.5	0.09	[24]
TAPC:TmPPPyTz	2.57	0.12	[24]
TCTA:TmPPPyTz	2.58	0.14	[24]
BF-DPB:B4PYMPM	2.49	0.11	[24]
m-MTDATA:B4PYMPM	2.15	0.19	[24]

References

(1) Byrnes, S. J. Multilayer Optical Calculations. *arXiv 1603 . 02720v3* **2018**, 1–20.

(2) De Mello, J. C.; Wittmann, H. F.; Friend, R. H. An Improved Experimental Determination of External Photoluminescence Quantum Efficiency. *Adv. Mater.* **1997**, *9* (3), 230–232. https://doi.org/10.1201/b10862-2.

(3) Goushi, K.; Yoshida, K.; Sato, K.; Adachi, C. Organic Light-Emitting Diodes Employing Efficient Reverse Intersystem Crossing for Triplet-to-Singlet State Conversion. *Nat. Photonics* **2012**, *6* (4), 253–258. https://doi.org/10.1038/nphoton.2012.31.

(4) Deotare, P. B.; Chang, W.; Hontz, E.; Congreve, D. N.; Shi, L.; Reusswig, P. D.; Modtland, B.; Bahlke, M. E.; Lee, C. K.; Willard, A. P.; Bulovic, V.; Van Voorhis, T.; Baldo, M. A. Nanoscale Transport of Charge-Transfer States in Organic Donor-Acceptor Blends. *Nat. Mater.* **2015**, *14* (11), 1130–1134. https://doi.org/10.1038/nmat4424.

(5) Ziffer, M. E.; Jo, S. B.; Zhong, H.; Ye, L.; Liu, H.; Lin, F.; Zhang, J.; Li, X.; Ade, H. W.; Jen, A. K.-Y.; Ginger, D. S. Long-Lived, Non-Geminate, Radiative Recombination of Photogenerated Charges in a Polymer/Small-Molecule Acceptor Photovoltaic Blend. *J. Am. Chem. Soc.* **2018**, *140* (31), 9996–10008. https://doi.org/10.1021/jacs.8b05834.

(6) Shockley, W.; Queisser, H. J. Detailed Balance Limit of Efficiency of P-n Junction Solar Cells. *J. Appl. Phys.* **1961**, *32* (3), 510–519. https://doi.org/10.1063/1.1736034.

(7) Azzouzi, M.; Yan, J.; Kirchartz, T.; Liu, K.; Wang, J.; Wu, H.; Nelson, J. Nonradiative Energy Losses in Bulk-Heterojunction Organic Photovoltaics. *Phys. Rev. X* **2018**, *8* (3), 031055. https://doi.org/10.1103/PhysRevX.8.031055.

(8) Yao, J.; Kirchartz, T.; Vezie, M. S.; Faist, M. A.; Gong, W.; He, Z.; Wu, H.; Troughton, J.; Watson, T.; Bryant, D.; Nelson, J. Quantifying Losses in Open-Circuit Voltage in Solution-Processable Solar Cells. *Phys. Rev. Appl.* **2015**, *014020*, 1–10. https://doi.org/10.1103/PhysRevApplied.4.014020.

(9) Rau, U.; Blank, B.; Müller, T. C. M.; Kirchartz, T.; Jülich, F. Efficiency Potential of Photovoltaic Materials and Devices Unveiled by Detailed-Balance Analysis. *Phys. Rev. Appl.* **2017**, No. 7, 044016. https://doi.org/10.1103/PhysRevApplied.7.044016.

(10) Rau, U. Reciprocity Relation between Photovoltaic Quantum Efficiency and Electroluminescent Emission of Solar Cells. *Phys. Rev. B* **2007**, *76* (8), 1–8. https://doi.org/10.1103/PhysRevB.76.085303.

(11) Coropceanu, V.; Chen, X.-K.; Wang, T.; Zheng, Z.; Brédas, J.-L. Charge-Transfer Electronic States in Organic Solar Cells. *Nat. Rev. Mater.* **2019**, *4* (11), 689–707. https://doi.org/10.1038/s41578-019-0137-9.

(12) Wang, Y.; Qian, D.; Cui, Y.; Zhang, H.; Hou, J.; Vandewal, K.; Kirchartz, T.; Gao, F. Optical Gaps of Organic Solar Cells as a Reference for Comparing Voltage Losses. *Adv. Energy Mater.* **2018**, 1801352. https://doi.org/10.1002/aenm.201801352.

(13) Azzouzi, M.; Yan, J.; Kirchartz, T.; Liu, K.; Wang, J.; Wu, H.; Nelson, J. Nonradiative Energy Losses in Bulk-Heterojunction Organic Photovoltaics. *Phys. Rev. X* **2018**, *8* (3), 1–14. https://doi.org/10.1103/PhysRevX.8.031055.

(14) Zhao, W.; Qian, D.; Zhang, S.; Li, S.; Inganäs, O.; Gao, F.; Hou, J. Fullerene-Free Polymer Solar Cells with over 11% Efficiency and Excellent Thermal Stability. *Adv. Mater.* **2016**, *28* (23), 4734–4739. https://doi.org/10.1002/adma.201600281.

(15) Qian, D.; Zheng, Z.; Yao, H.; Tress, W.; Hopper, T. R.; Chen, S.; Li, S.; Liu, J.; Chen, S.; Zhang, J.; Liu, X.-K.; Gao, B.; Ouyang, L.; Jin, Y.; Pozina, G.; Buyanova, I. A.; Chen, W. M.; Inganäs, O.; Coropceanu, V.; Bredas, J.-L.; Yan, H.; Hou, J.; Zhang, F.; Bakulin, A. A.; Gao, F. Design Rules for Minimizing Voltage Losses in High-Efficiency Organic Solar Cells. *Nat. Mater.* **2018**, *17* (8), 703–709. https://doi.org/10.1038/s41563-018-0128-z.

(16) Zhang, J.; Kan, B.; Pearson, A. J.; Parnell, A. J.; Cooper, J. F. K.; Liu, X. K.; Conaghan, P. J.; Hopper, T. R.; Wu, Y.; Wan, X.; Gao, F.; Greenham, N. C.; Bakulin, A. A.; Chen, Y.; Friend, R. H. Efficient Non-Fullerene Organic Solar Cells Employing Sequentially Deposited Donor-Acceptor Layers. *J. Mater. Chem. A* **2018**, *6* (37), 18225–18233. https://doi.org/10.1039/c8ta06860g.

(17) Liu, J.; Chen, S.; Qian, D.; Gautam, B.; Yang, G.; Zhao, J.; Bergqvist, J.; Zhang, F.; Ma, W.; Ade, H.; Inganäs, O.; Gundogdu, K.; Gao, F.; Yan, H. Fast Charge Separation in a Non-Fullerene Organic Solar Cell with a Small Driving Force. *Nat. Energy* **2016**, *1* (7), 16089–16095. https://doi.org/10.1038/nenergy.2016.89.

(18) Liu, S.; Yuan, J.; Deng, W.; Luo, M.; Xie, Y.; Liang, Q.; Zou, Y.; He, Z.; Wu, H.; Cao, Y. High-Efficiency Organic Solar Cells with Low Non-Radiative Recombination Loss and Low Energetic Disorder. *Nat. Photonics* **2020**, *14* (5), 300–305. https://doi.org/10.1038/s41566-019-0573-5.

(19) Liu, X.; Du, X.; Wang, J.; Duan, C.; Tang, X.; Heumueller, T.; Liu, G.; Li, Y.; Wang, Z.; Wang, J.; Liu, F.; Li, N.; Brabec, C. J.; Huang, F.; Cao, Y. Efficient Organic Solar Cells with Extremely High Open-Circuit Voltages and Low Voltage Losses by Suppressing Nonradiative Recombination Losses. *Adv. Energy Mater.* **2018**, *8* (26), 1–9. https://doi.org/10.1002/aenm.201801699.

(20) Eisner, F. D.; Azzouzi, M.; Fei, Z.; Hou, X.; Anthopoulos, T. D.; Dennis, T. J. S.; Heeney, M.; Nelson, J. Hybridization of Local Exciton and Charge-Transfer States Reduces Nonradiative Voltage Losses in Organic Solar Cells. *J Am Chem Soc* **2019**, *141*, 6362–6374. https://doi.org/10.1021/jacs.9b01465.

(21) Ran, N. A.; Love, J. A.; Takacs, C. J.; Sadhanala, A.; Beavers, J. K.; Collins, S. D.; Huang,

Y.; Wang, M.; Friend, R. H.; Bazan, G. C. Harvesting the Full Potential of Photons with Organic Solar Cells. *Adv. Mater.* **2016**, 1482–1488. https://doi.org/10.1002/adma.201504417.

(22) Wang, C.; Xu, X.; Zhang, W.; Bergqvist, J.; Xia, Y.; Meng, X.; Bini, K.; Ma, W.; Yartsev, A.; Vandewal, K.; Andersson, M. R.; Inganäs, O.; Fahlman, M.; Wang, E. Low Band Gap Polymer Solar Cells With Minimal Voltage Losses. *Adv. Energy Mater.* **2016**, *6* (18), 1–10. https://doi.org/10.1002/aenm.201600148.

(23) Benduhn, J.; Tvingstedt, K.; Piersimoni, F.; Ullbrich, S.; Fan, Y.; Tropiano, M.; McGarry, K. A.; Zeika, O.; Riede, M. K.; Douglas, C. J.; Barlow, S.; Marder, S. R.; Neher, D.; Spoltore, D.; Vandewal, K. Intrinsic Non-Radiative Voltage Losses in Fullerene-Based Organic Solar Cells. *Nat. Energy* **2017**, *2* (6), 17053. https://doi.org/10.1038/nenergy.2017.53.

(24) Ullbrich, S.; Benduhn, J.; Jia, X.; Nikolis, V. C.; Tvingstedt, K.; Piersimoni, F.; Roland, S.; Liu, Y.; Wu, J.; Fischer, A.; Neher, D.; Reineke, S.; Spoltore, D.; Vandewal, K. Emissive and Charge-Generating Donor–Acceptor Interfaces for Organic Optoelectronics with Low Voltage Losses. *Nat. Mater.* **2019**, *18* (5), 459–464. https://doi.org/10.1038/s41563-019-0324-5.

(25) Jorgensen, W. L.; Maxwell, D. S.; Tirado-Rives, J. Development and Testing of the OPLS All-Atom Force Field on Conformational Energetics and Properties of Organic Liquids. *J. Am. Chem. Soc.* **1996**, *118* (45), 11225–11236. https://doi.org/10.1021/ja9621760.

(26) Wunsch, B. H.; Rumi, M.; Tummala, N. R.; Risko, C.; Kang, D. Y.; Steirer, K. X.; Gantz, J.; Said, M.; Armstrong, N. R.; Brédas, J. L.; Bucknall, D.; Marder, S. R. Structure-Processing-Property Correlations in Solution-Processed, Small-Molecule, Organic Solar Cells. *J. Mater. Chem. C* **2013**, *1* (34), 5250–5260. https://doi.org/10.1039/c3tc30774c.

(27) Kronik, L.; Stein, T.; Refaely-Abramson, S.; Baer, R. Excitation Gaps of Finite-Sized Systems from Optimally Tuned Range-Separated Hybrid Functionals. *J. Chem. Theory Comput.* **2012**, *8* (5), 1515–1531. https://doi.org/10.1021/ct2009363.

(28) Voityuk, A. A.; Rösch, N. Fragment Charge Difference Method for Estimating Donor-Acceptor Electronic Coupling: Application to DNA π-Stacks. *J. Chem. Phys.* **2002**, *117* (12), 5607–5616. https://doi.org/10.1063/1.1502255.

(29) Hess, B.; Kutzner, C.; Van Der Spoel, D.; Lindahl, E. GRGMACS 4: Algorithms for Highly Efficient, Load-Balanced, and Scalable Molecular Simulation. *J. Chem. Theory Comput.* **2008**, *4* (3), 435–447. https://doi.org/10.1021/ct700301q.

(30) Berendsen, H. J. C.; van der Spoel, D.; van Drunen, R. GROMACS: A Message-Passing Parallel Molecular Dynamics Implementation. *Comput. Phys. Commun.* **1995**, *91* (1–3), 43–56. https://doi.org/10.1016/0010-4655(95)00042-E.

(31) Kahle, F. J.; Rudnick, A.; Bässler, H.; Köhler, A. How to Interpret Absorption and Fluorescence Spectra of Charge Transfer States in an Organic Solar Cell. *Mater. Horizons* **2018**, *5* (5), 837–848. https://doi.org/10.1039/c8mh00564h.

(32) Zheng, Z.; Tummala, N. R.; Wang, T.; Coropceanu, V.; Brédas, J.-L. Charge-Transfer

States at Organic–Organic Interfaces: Impact of Static and Dynamic Disorders. *Adv. Energy Mater.* **2019**, *9* (14), 1803926. https://doi.org/10.1002/aenm.201803926.

(33) Burke, T. M.; Sweetnam, S.; Vandewal, K.; McGehee, M. D. Beyond Langevin Recombination: How Equilibrium Between Free Carriers and Charge Transfer States Determines the Open-Circuit Voltage of Organic Solar Cells. *Adv. Energy Mater.* **2015**, *5* (11), 1500123. https://doi.org/10.1002/aenm.201500123.

(34) Sulas, D. B.; Rabe, E. J.; Schlenker, C. W. Kinetic Competition between Charge Separation and Triplet Formation in Small-Molecule Photovoltaic Blends. *J. Phys. Chem. C* **2017**, *121* (48), 26667–26676. https://doi.org/10.1021/acs.jpcc.7b09365.

(35) Qian, D.; Zheng, Z.; Yao, H.; Tress, W.; Hopper, T. R.; Chen, S.; Li, S.; Liu, J.; Chen, S.; Zhang, J.; Liu, X. K.; Gao, B.; Ouyang, L.; Jin, Y.; Pozina, G.; Buyanova, I. A.; Chen, W. M.; Inganäs, O.; Coropceanu, V.; Bredas, J. L.; Yan, H.; Hou, J.; Zhang, F.; Bakulin, A. A.; Gao, F. Design Rules for Minimizing Voltage Losses in High-Efficiency Organic Solar Cells. *Nat. Mater.* **2018**, *17* (8), 703–709. https://doi.org/10.1038/s41563-018-0128-z.

(36) Liu, J.; Chen, S. S.; Qian, D. P.; Gautam, B.; Yang, G. F.; Zhao, J. B.; Bergqvist, J.; Zhang, F. L.; Ma, W.; Ade, H.; Inganas, O.; Gundogdu, K.; Gao, F.; Yan, H. Fast Charge Separation in a Non-Fullerene Organic Solar Cell with a Small Driving Force. *Nat. Energy* **2016**, *1*. https://doi.org/Artn 16089 10.1038/Nenergy.2016.89.

(37) Cui, Y.; Yao, H.; Zhang, J.; Zhang, T.; Wang, Y.; Hong, L.; Xian, K.; Xu, B.; Zhang, S.; Peng, J.; Wei, Z.; Gao, F.; Hou, J. Over 16% Efficiency Organic Photovoltaic Cells Enabled by a Chlorinated Acceptor with Increased Open-Circuit Voltages. *Nat. Commun.* **2019**, *10* (1), 2515. https://doi.org/10.1038/s41467-019-10351-5.